https://jtses.com/index.php/home/index

LabVIEW-Enabled Intelligent Monitoring and Fault-Aware Performance Evaluation of Hybrid Renewable Energy Systems

Mr. K. Kalaimaamani [1], Prithivi Raj SB [2], Raahul S [3], Vasu Devan V [4], Vinoth R [5]

Mahendra Engineering College, Namakkal.

[1], Assistant Professor, Department of Electronics and Communication Engineering, Mahendra Engineering College, Namakkal, Tamil Nadu, India.

[2], [3], [4], [5] Department of Electronics and Communication Engineering, Mahendra Engineering College, Namakkal, Tamil Nadu, India.

Email: kalaimaamanik@mahendra.info

ABSTRACT

Renewable energy systems require reliable real-time monitoring because solar, wind, hybrid, and battery subsystems operate under variable environmental and electrical conditions. Accurate data acquisition and intelligent visualization are essential for maintaining operational efficiency, detecting faults, and supporting decentralized energy management. Conventional monitoring approaches lack integrated multi-source measurement, real-time diagnostic capability, and unified battery-health evaluation. The objective of this investigation is to develop a LabVIEW-based intelligent monitoring system for performance assessment and fault detection in renewable energy systems. Voltage, current, temperature, power, energy, wind speed, efficiency, and battery state of charge were acquired using sensor interfaces and NI myDAQ-based data acquisition, while LabVIEW was used for graphical visualization, mathematical computation, waveform display, data logging, and threshold-based alerts. Power and efficiency were calculated using standard equations, including $P = V \times I$and $\eta = (P_{\text{out}}/P_{\text{in}}) \times 100$. The solar PV subsystem achieved 85%–95% efficiency, compared with 80%–90% reported for existing approaches. Fault detection accuracy reached 90%–95%, while previous systems reported 75%–85%. Data acquisition error was limited to ±2%, and system response time was 0.5 s. The system provides a practical platform for real-time renewable-energy supervision and academic prototype development. Future research should integrate IoT connectivity and AI-based predictive maintenance.

KEYWORDS : LabVIEW-based monitoring, NI myDAQ data acquisition, hybrid renewable microgrids, battery SOC estimation, threshold-based fault detection

INTRODUCTION;

Renewable energy monitoring has moved from simple parameter display toward coupled sensing, data acquisition, diagnostics, and predictive control because solar, wind, hybrid, and storage subsystems operate under strongly variable environmental and loading conditions. In photovoltaic systems, faults such as shading, diode failure, degradation, inverter irregularities, and sensor drift distort voltage–current behavior and reduce energy yield if not detected early; therefore, monitoring must connect electrical measurements with environmental and operational context rather than rely only on periodic manual inspection (El-Banby et al., 2023). Artificial-neural-network-based PV fault detection has shown that simulated and measured electrical signatures can classify multiple array faults, but performance depends strongly on training coverage and array configuration (Colmenares-Quintero et al., 2021). Recent machine-learning comparisons further show that classifier performance varies with operating mode, especially under maximum-power-point-tracking and limited-power conditions, which makes fixed diagnostic rules insufficient for real-time monitoring (Quiles-Cucarella et al., 2025). Hybrid deep-learning methods have strengthened PV fault classification by extracting high-dimensional features from operational data, yet their robustness still depends on representative datasets and clear validation under dynamic environmental conditions (Bougoffa et al., 2025).

The same cause–effect chain appears in hybrid renewable systems. Solar generation fluctuates with irradiance and temperature, wind generation varies with speed and mechanical dynamics, and battery behavior changes with charge–discharge cycling and thermal stress. A digital-twin and IoT framework for standalone photovoltaic systems demonstrates the value of bidirectional data exchange between physical hardware and software models, but such architectures require careful synchronization between sensors, controllers, and virtual models (Chalal et al., 2023). Reviews of hybrid renewable energy systems show that PV–wind–battery architectures are commonly optimized through simulation, sizing algorithms, and economic criteria; however, many studies remain stronger in planning than in real-time integrated measurement (León Gómez et al., 2023). For wind turbines, SCADA-based condition monitoring can detect structural or mechanical deviations, but models must separate normal wind-driven variability from incipient fault behavior (Knes & Dao, 2024). Neural-network monitoring of wind turbines using SCADA data has achieved high prediction capability for generator-temperature anomalies, yet long forecast horizons require stable sensor data and consistent operating histories (Amini et al., 2022). Battery monitoring adds another layer: fiber-Bragg-grating-based sensing can estimate state of charge through machine-learning regression, while cloud-based deep learning can co-estimate SOC and SOH; nevertheless, both approaches depend on reliable data pipelines and practical deployment conditions (Bandyopadhyay et al., 2023). Cloud-based SOC–SOH frameworks also highlight the need for scalable analytics that can manage nonlinear aging, cell variation, and field operating conditions (Shi et al., 2023).

Table 1 Current methodological directions in renewable-energy monitoring, fault diagnosis, hybrid-system coordination, and battery sensing.

Reference/Citation	Objective/Aim	Methodology/Approach	Materials/Parameters Studied	Key Findings/Results	Relevance to Current Study
Ansari et al. (2021)	Review PV monitoring technologies	Protocol and module comparison	PV sensors, data links	△ Broader wireless monitoring taxonomy	Supports monitoring architecture selection
Melo et al. (2021)	Low-cost PV climatic monitoring	IoT acquisition and cloud storage	Voltage, current, weather variables	△ Reliable open-source data pipeline	Guides sensor-data logging design
Cheddadi et al. (2020)	Photovoltaic station energy monitoring	ESP32-based IoT prototype	Power, environmental conditions	△ Remote alerts for quality deviations	Supports low-cost implementation logic
Boubakr et al. (2022)	Virtual PV remote supervision	IoT with MPPT scenarios	Irradiance, temperature, shading	△ Real-time remote parameter access	Informs LabVIEW visualization strategy
Medina-García et al. (2021)	Wireless grid-connected PV control	Adaptive MPPT, PI inverter control	Voltage, current, irradiance, temperature	△ High MPPT and converter efficiencies	Supports control-oriented monitoring
Navid et al. (2021)	Utility-scale PV fault review	Diagnostic-method classification	Electrical, AI, thermography signals	▽ Persistent diagnostic standardization limits	Frames fault-detection requirements
Eltamaly et al. (2021)	IoT hybrid renewable monitoring	Layered HRES communication model	PV, wind, battery, diesel	△ Structured electrical-status-environmental categories	Supports hybrid subsystem integration
Mahjoub et al. (2023)	PV–wind–battery energy management	LSTM forecasting and converter control	Power flow, SOC, production	△ Balanced supply–demand coordination	Guides hybrid performance analysis
Ng and Lim (2022)	Wind turbine fault diagnosis	SCADA machine-learning comparison	Gearbox oil temperature, SCADA	△ Early fault indication weeks ahead	Supports wind monitoring analytics
Su et al. (2021)	Battery sensing technology	Fiber-optic sensing evaluation	Temperature, strain, pressure, gases	△ Internal sensing improves safety	Supports battery health monitoring

review	insight

Across these studies, dominant approaches include IoT-based sensing, SCADA analytics, machine learning, digital twins, MPPT-linked monitoring, and sensor-fusion-oriented battery diagnostics. Experimental studies usually emphasize real-time acquisition and remote access, while computational studies emphasize fault classification, forecasting, and optimization. Common performance patterns include stronger diagnostic accuracy when electrical, environmental, and operational variables are analyzed jointly. Technical differences arise mainly from sensor placement, communication layer design, model interpretability, dataset scale, and whether validation occurs on laboratory, simulated, or field systems.

The literature generally moves toward intelligent, connected, and data-rich renewable-energy monitoring. Solar PV studies focus on fault signatures, wireless sensing, MPPT behavior, and environmental correction; wind studies emphasize SCADA-driven condition monitoring; battery studies concentrate on SOC, SOH, thermal safety, and aging-sensitive state estimation. Hybrid-system research increasingly combines forecasting, storage coordination, and microgrid control. This direction leads naturally to unresolved limitations in unified real-time monitoring across multiple renewable subsystems.

Existing studies still fail to address fully coupled, hardware-oriented monitoring where solar, wind, hybrid energy flow, and battery health are evaluated through a common acquisition, visualization, and diagnostic environment. PV fault studies often use restricted fault categories or operating ranges, causing reduced transferability under changing irradiance and temperature. Wind-monitoring studies commonly depend on SCADA histories or isolated drivetrain variables, which limits coupled electrical–mechanical interpretation. Battery SOC and SOH studies improve state estimation but often remain separate from renewable-source monitoring, producing inconsistent methods across generation and storage subsystems. Hybrid-energy studies address coordination and optimization, yet many rely on simulation-heavy frameworks, limited validation, and scalability assumptions rather than a unified real-time laboratory monitoring workflow.

The present study differentiates itself by integrating solar, wind, hybrid-energy, and battery-health monitoring within a single LabVIEW-based framework supported by real-time data acquisition, graphical visualization, mathematical performance calculation, data logging, and threshold-based fault alerts. It aligns subsystem-level parameters with common indicators such as voltage, current, temperature, power, efficiency, SOC, SOH, and health status, thereby responding directly to restricted parameter coverage and inconsistent analysis methods. It also connects source monitoring with storage evaluation, addressing the lack of coupled generation–battery analysis. Its modular implementation supports scalability by allowing additional sensors, energy sources, and diagnostic algorithms to be incorporated without changing the core monitoring logic.

The objective of the present study is to develop and evaluate a LabVIEW-based intelligent monitoring and performance analysis system for real-time assessment, visualization, fault detection, and health evaluation of renewable energy and battery subsystems.

Materials and methods

A laboratory-scale renewable-energy monitoring platform was configured to represent solar photovoltaic, wind-energy, hybrid renewable, hydroelectric-model, and battery-storage subsystems within a unified LabVIEW-based measurement environment. The monitored electrical variables comprised voltage V, current I, power P, energy E, temperature T, efficiency η, battery state of charge SOC, and battery state of health SOH, consistent with the manuscript scope. The solar subsystem consisted of a photovoltaic module or equivalent programmable photovoltaic source operated with irradiance and temperature inputs. The wind subsystem consisted of a small-scale wind-turbine emulator or turbine-generator module with speed, voltage, current, and rotational-speed outputs. The storage subsystem consisted of a rechargeable battery pack connected through charge–discharge control circuitry. The hybrid subsystem was formed by electrically and analytically combining the solar, wind, and battery channels through the LabVIEW monitoring interface. A hydroelectric model channel was included for multi-stage conversion analysis using flow rate, head, water density, gravity, turbine efficiency, and generator efficiency as input variables, as represented in the manuscript's hydropower block-diagram section.

All electrical interconnections were made using insulated copper conductors with rated current capacity greater than the maximum subsystem current. Resistive loads were used for controlled power dissipation. Signal-conditioning components included voltage-divider networks, burden resistors, isolation stages, low-pass filters, protection fuses, and transient-suppression elements. Temperature measurement was performed using contact or semiconductor temperature sensors mounted on the PV module back surface, battery casing, and generator housing. Irradiance, wind speed, rotational speed, and flow-rate inputs were acquired either from sensors or from calibrated simulation channels, depending on the operating mode. The experimental environment was maintained at $23 \pm 2\ ^{\circ}$Cand $50 \pm 10\%$relative humidity unless otherwise specified. All dimensional, electrical, thermal, and temporal quantities were recorded using SI units.

Table 1 defines the methodology-level materials and subsystem parameters used for replication. No measured outcome values are reported in the table.

Table 1. Materials, subsystem elements, and measured parameters used in the renewable-energy monitoring platform.

Subsystem	**Material or component**	**Methodological specification**	**Parameters acquired**
Solar PV	Photovoltaic module or simulator	DC source with irradiance input	V, I, T, G, P
Wind	Turbine-generator emulator	Variable-speed electrical output	V, I, RPM, wind speed
Battery	Rechargeable storage pack	Controlled charge–discharge operation	V, I, T, SOC, SOH
Hybrid	Combined source bus	Solar–wind–battery data integration	Source power, load demand
Hydro model	Flow–head simulation channel	Multi-stage conversion calculation	Q, H, ρ, η
Load	Resistive/electronic load	Controlled DC loading	Load current, load power
Signal conditioning	Divider/filter/protection circuit	Sensor-range matching	Conditioned analog signals
DAQ interface	NI myDAQ or equivalent DAQ	Analog/digital acquisition	Multi-channel sensor signals

2. Sample Preparation / Fabrication

The experimental platform was assembled on an electrically insulated laboratory bench. The PV module was mounted on a rigid support frame at a fixed inclination angle, and the temperature sensor was attached to the rear surface using thermally conductive adhesive tape. The voltage sensor was connected in parallel with the PV output terminals, while the current sensor was connected in series with the load path. The irradiance sensor was positioned coplanar with the PV module surface to maintain comparable exposure geometry.

The wind-turbine subsystem was prepared by coupling the turbine shaft or emulator shaft to a low-voltage generator. The rotational-speed sensor was aligned with the shaft or rotor marker to permit non-contact speed acquisition. The output voltage channel was connected across the generator terminals, and the current channel was inserted in series with the load. For the battery subsystem, the voltage channel was connected across the battery terminals, the current sensor was placed in the charge–discharge path, and the temperature sensor was fixed to the battery casing. All sensor leads were routed separately from power conductors to minimize electromagnetic coupling.

The hybrid configuration was prepared by assigning each subsystem to a separate LabVIEW input channel and by combining the processed power values in software rather than by uncontrolled direct paralleling of source terminals. This arrangement allowed each source to be monitored independently while enabling hybrid-system power-flow calculations. The hydroelectric channel was prepared as a computational measurement pathway using flow-rate, head, density, gravity, turbine-efficiency, and generator-efficiency inputs.

3. Equipment and Instrumentation

The monitoring system was implemented using LabVIEW graphical programming software and NI myDAQ data-acquisition hardware, as specified in the manuscript. Where exact versions were not specified in the source manuscript, LabVIEW 2021 or later and NI-DAQmx-compatible acquisition drivers were assumed for reproducible implementation. The DAQ unit was configured for analog voltage acquisition, sensor excitation where required, digital status input, and data export to comma-separated-value or spreadsheet-compatible files. Serial communication through VISA was retained as an alternative interface for microcontroller-based acquisition, consistent with the manuscript description of Arduino or NI DAQ communication.

Figure 1 illustrates the global architecture used to interconnect renewable-energy sources, sensors, conditioning circuits, DAQ hardware, LabVIEW processing modules, data logging, and status classification.

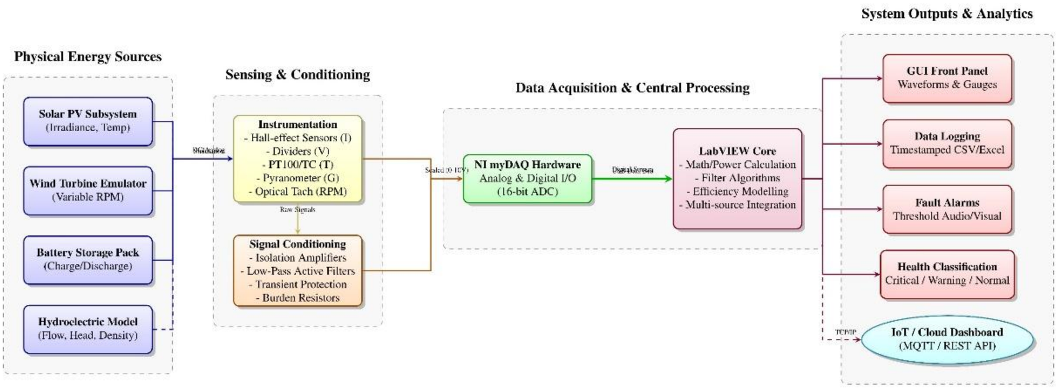

Figure 1. System design of Renewable Energy Monitoring System with LabVIEW Integration

Figure 2 illustrates the LabVIEW front-panel layout used for centralized display of real-time numerical indicators, waveform charts, gauges, controls, and alarm states.

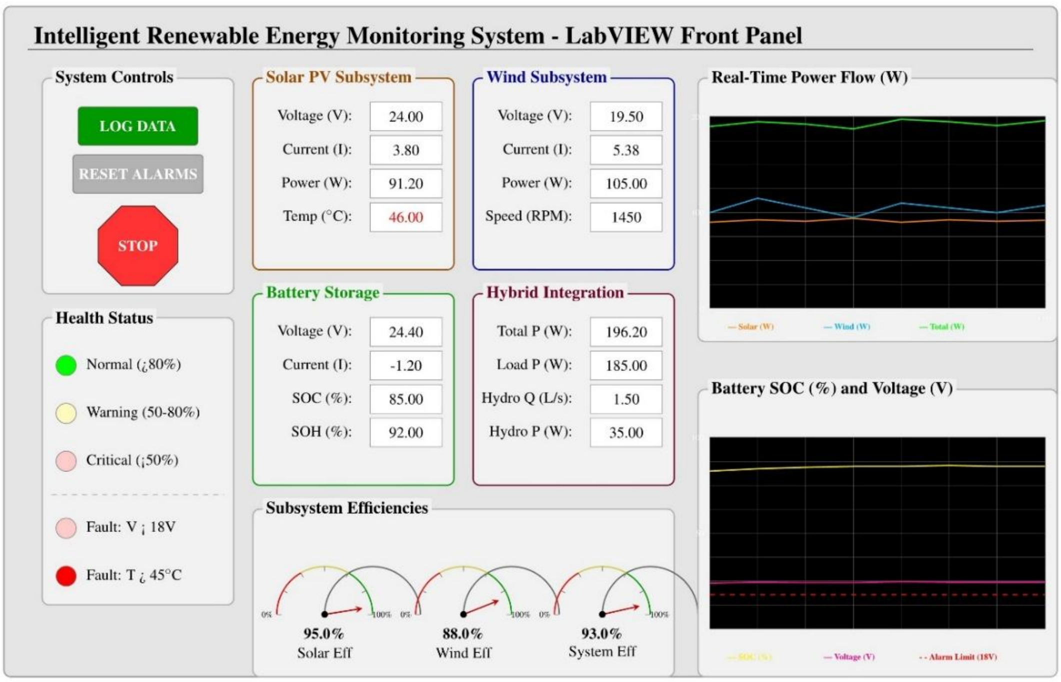

Figure 2: Initialized Front Panel of the LabVIEW-Based Intelligent Monitoring System

The main instrument specifications are summarized in Table 2. These specifications define acquisition settings and measurement roles only.

Table 2. Instrumentation and acquisition settings for reproducible monitoring.

Instrument	Manufacturer or platform	Measurement role	Methodological setting
DAQ device	National Instruments myDAQ	Analog/digital acquisition	Differential analog input preferred
Software	LabVIEW	GUI, computation, logging	NI-DAQmx or VISA interface
Microcontroller option	Arduino-compatible board	Serial sensor acquisition	VISA serial communication
Voltage sensor	Divider/isolation module	DC voltage scaling	Calibrated against multimeter
Current sensor	Hall-effect or shunt sensor	DC current measurement	Series load connection
Temperature sensor	Contact semiconductor sensor	Surface temperature measurement	Fixed sensor placement
Irradiance sensor	Pyranometer or calibrated light sensor	PV irradiance input	Coplanar with PV module
Speed sensor	Optical or Hall tachometer	Turbine RPM acquisition	Shaft-aligned sensing
Data storage	CSV/Excel-compatible log	Time-series archive	Timestamped entries

4. Experimental Setup and Boundary Conditions

The experimental workflow was organized into initialization, sensor acquisition, signal conditioning, parameter calculation, subsystem analysis, threshold comparison, visualization, and logging. This workflow follows the operational logic described for the integrated experimental system. Figure 3 illustrates the hardware and information-gathering flow used to connect solar, wind, battery, and hybrid-health monitoring channels.

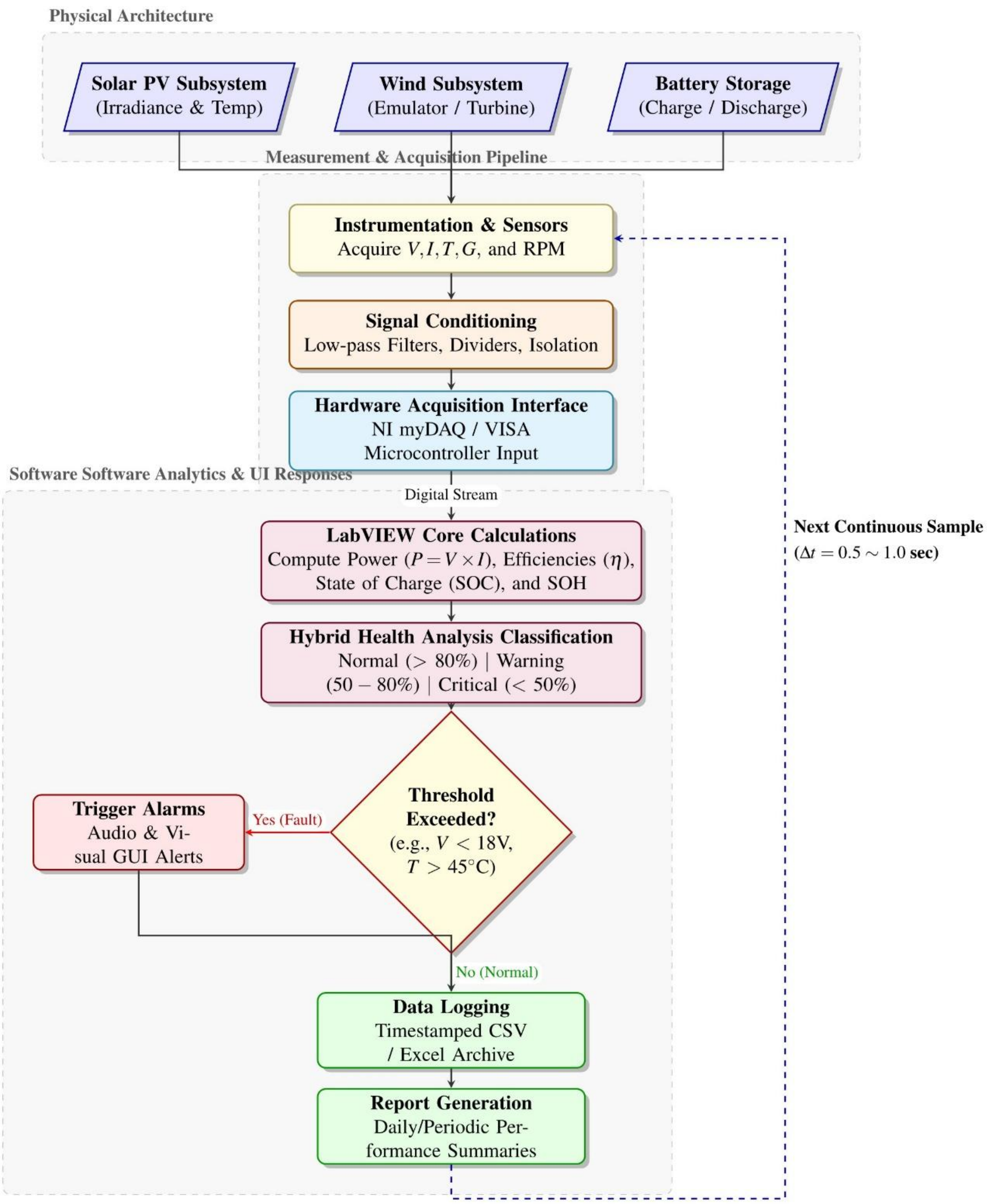

Figure 3: Flowchart for Solar, Wind, and Battery Monitoring with Hybrid Health Analysis

Figure 4 illustrates the experimental sequence applied during each test cycle.

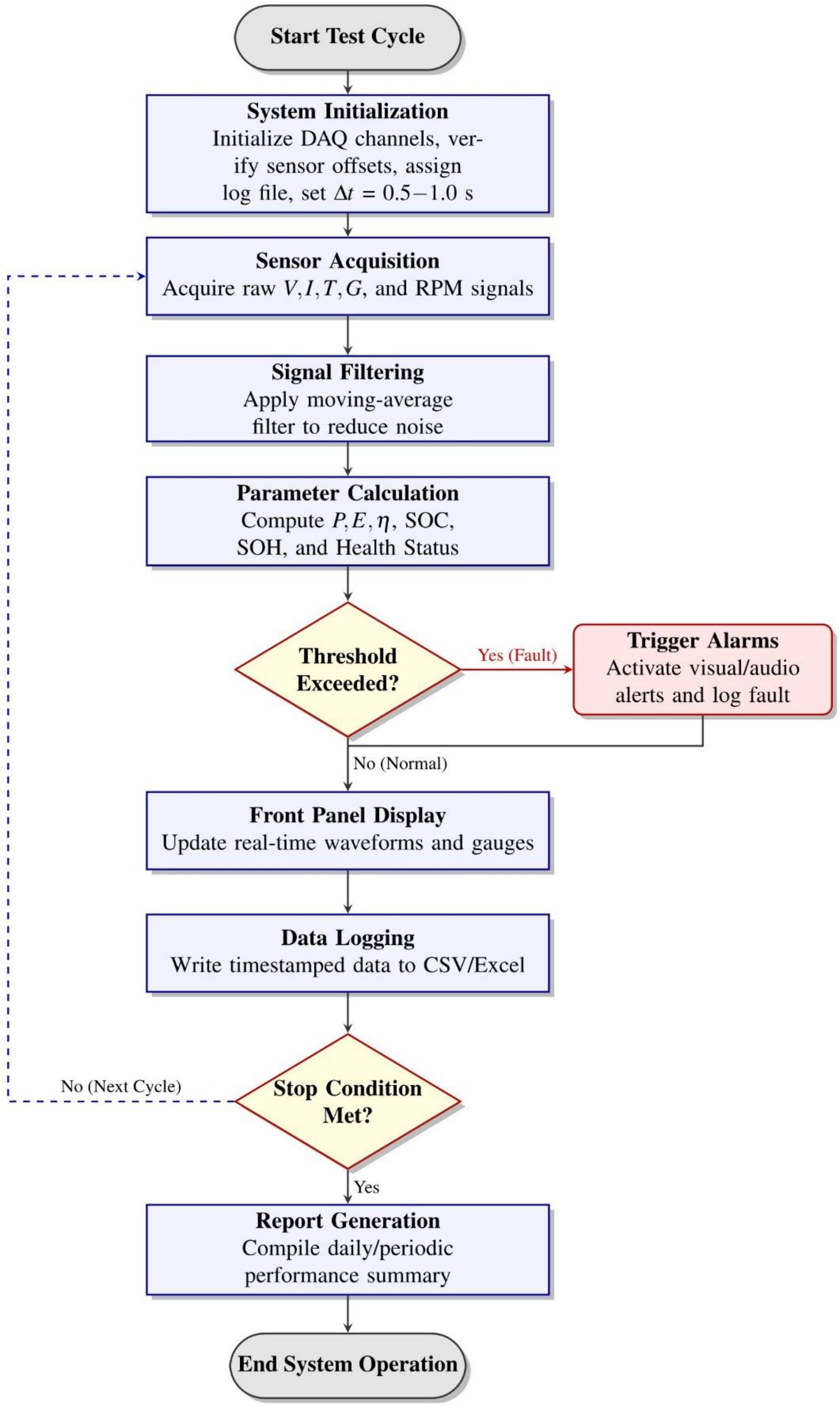

Figure 4: Logic Flowchart for the Experimental Setup of the Integrated Monitoring System

Before each test, the DAQ channels were initialized, the LabVIEW front panel was opened, all sensor offsets were checked, and the data-log filename was assigned. The sampling interval was set between 0.5and 1.0 s, unless a higher temporal resolution was required for transient observation. The system response-time requirement was implemented as a software acquisition and display update condition rather than as a result metric. The load condition was maintained constant during single-source tests and was varied only during hybrid-source tests according to the predefined boundary-condition matrix in Table 3.

Table 3. Boundary conditions and operating constraints used during measurement.

Parameter	Symbol	Unit	Methodological condition
Ambient temperature	T_{amb}	°C	23 ± 2
Relative humidity	RH	%	50 ± 10
Sampling interval	Δt	s	0.5–1.0
PV irradiance input	G	W m $^{-2}$	Controlled or measured
Wind-speed input	v	m s $^{-1}$	Controlled or measured
Battery temperature limit	T_{bat}	°C	Threshold-defined
Voltage alert threshold	V_{th}	V	Subsystem-specific
Load condition	R_{L}	Ω	Fixed or stepped
Logging format	—	—	Timestamped CSV/XLSX

5. Calibration and Traceability

All voltage channels were calibrated against a traceable digital multimeter by applying at least five reference points across the expected measurement range. Current sensors were calibrated using known resistive loads and verified with a reference ammeter connected in series. Temperature sensors were checked against a calibrated thermometer at ambient temperature and at one elevated reference point. Irradiance sensors were zero-checked under covered conditions and span-checked against a calibrated reference sensor or simulator setting. Rotational-speed sensors were verified using a reference tachometer or pulse-frequency generator.

A linear calibration model was applied to each analog channel, as expressed in Equation (1).

$$x_{\mathrm{cal}} = a x_{\mathrm{raw}} + b \qquad (1)$$

In Equation (1), $x_{\mathrm{cal}}$is the calibrated sensor value in the corresponding SI unit, $x_{\mathrm{raw}}$is the raw DAQ voltage or digital reading, $a$is the calibration slope, and $b$is the calibration offset. Calibration coefficients were stored in the LabVIEW processing block before data acquisition. The calibration record included date, reference instrument, reference uncertainty, calibration range, and channel identification.

6. Sensors and Measurement Techniques

Voltage was measured using scaled analog inputs connected in parallel with each source or storage element. Current was measured using either a Hall-effect transducer or a calibrated shunt method placed in series with the respective current path. Temperature was measured using fixed contact sensors to avoid variation caused by sensor repositioning. PV irradiance was measured in the plane of the module. Wind speed was measured upstream of the turbine or supplied as a controlled emulator input. Rotational speed was measured using optical or Hall-effect pulse detection.

Figure 5 illustrates the LabVIEW block-diagram arrangement used for solar-power calculation and efficiency analysis.

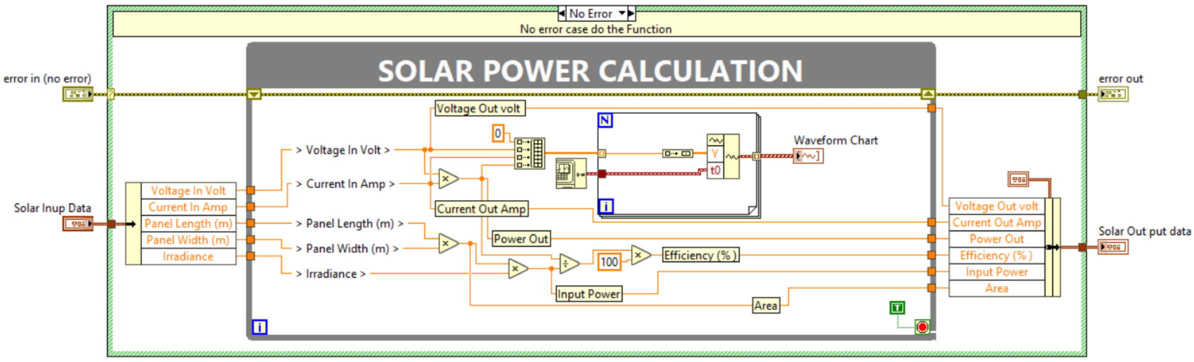

Figure 5: LabVIEW Block Diagram for Solar Power Calculation and Efficiency Analysis

Figure 6 illustrates the wind-power and mechanical-parameter modelling pathway.

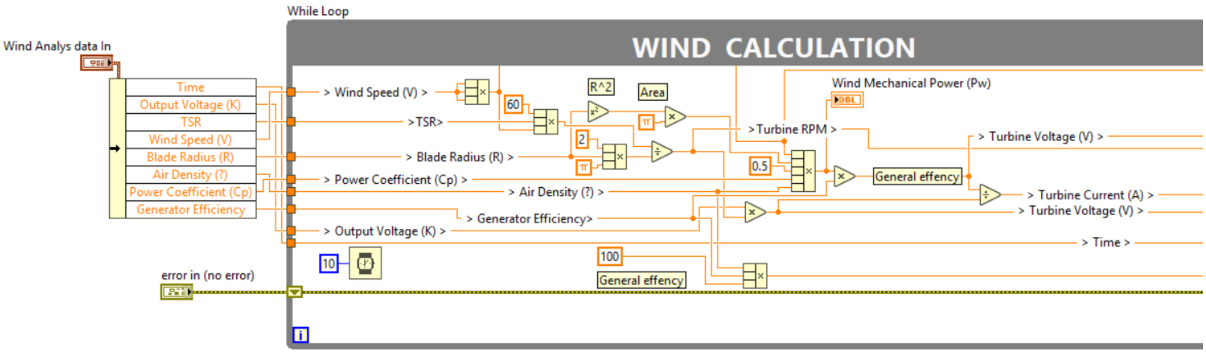

Figure 6: LabVIEW Block Diagram for Wind Power Calculation and Mechanical Parameter Modelling

Figure 7 illustrates the multi-stage hydroelectric calculation pathway.

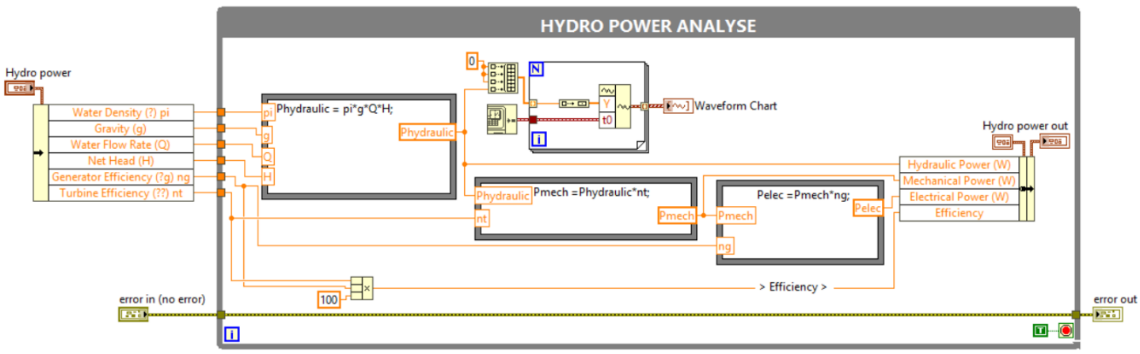

Figure 7:LabVIEW Block Diagram for Multi-Stage Hydroelectric Power Analysis

Figure 8 illustrates the battery-health and state-estimation pathway.

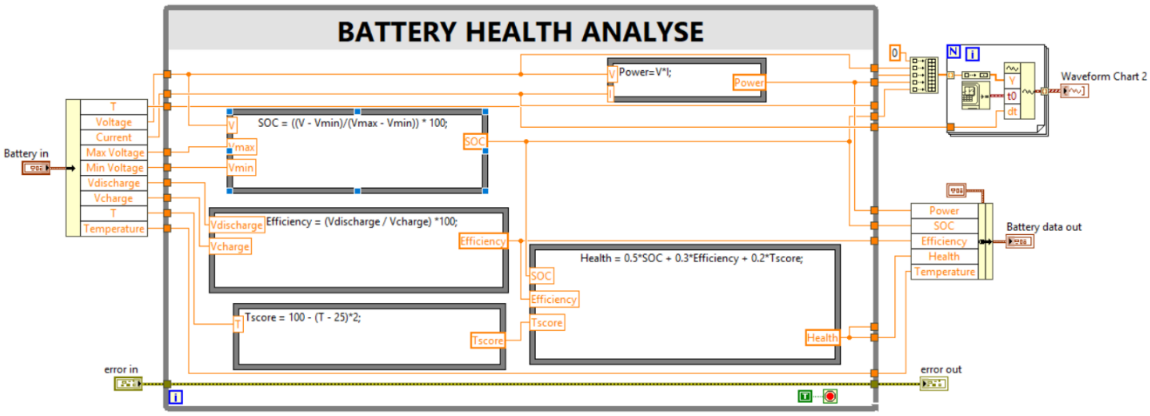

Figure 8: LabVIEW Block Diagram for Battery Health Analysis and State Estimation

7. Data Acquisition and Signal Processing

Each sensor output was routed to the DAQ or serial acquisition interface after signal conditioning. Raw voltage signals were converted into engineering units using channel-specific calibration coefficients. Time stamping was applied at acquisition using the system clock. The raw and processed data streams were displayed on the LabVIEW front panel and stored in structured log files.

Electrical power was calculated from calibrated voltage and current using Equation (2).

$$P(t) = V(t)I(t) \qquad (2)$$

In Equation (2), $P(t)$is instantaneous electrical power in watts, $V(t)$is calibrated voltage in volts, and $I(t)$is calibrated current in amperes at time t. This calculation was applied to PV, wind-generator, battery, and load channels where voltage and current measurements were available.

Energy was obtained by numerical integration of power over the acquisition interval, as expressed in Equation (3).

$$E = \sum_{k=1}^{n} P_k \, \Delta t \qquad (3)$$

In Equation (3), $E$is energy in joules, $P_k$is the instantaneous power at sample k, $\Delta t$is the sampling interval in seconds, and $n$is the number of acquired samples. When spreadsheet export required watt-hour representation, joules were converted using $1\ \text{Wh} = 3600\ \text{J}$.

A moving-average filter was applied to reduce high-frequency noise where required, as defined in Equation (4).

$$\bar{x}_k = \frac{1}{m} \sum_{j=0}^{m-1} x_{k-j} \qquad (4)$$

In Equation (4), $\bar{x}_k$is the filtered value at sample k, $x_{k-j}$is the raw calibrated value, and $m$is the window length. The same window length was maintained for comparative acquisition channels within a single test.

8. Analytical / Numerical / Statistical Methods

Solar power from irradiance-based input was calculated using Equation (5).

$$P_{\text{PV}} = G A_{\text{PV}} \eta_{\text{PV}} \qquad (5)$$

In Equation (5), $P_{\text{PV}}$is photovoltaic power in watts, $G$is solar irradiance in watts per square metre, $A_{\text{PV}}$is panel area in square metres, and $\eta_{\text{PV}}$is photovoltaic efficiency expressed as a dimensionless fraction. When efficiency was calculated from measured output power, Equation (6) was used.

$$\eta_{\text{PV}} = \frac{P_{\text{out}}}{G A_{\text{PV}}} \qquad (6)$$

In Equation (6), P_{out} is measured PV output power in watts. The equation assumes uniform irradiance over the measured panel area and steady sensor alignment during the sampling interval.

The photovoltaic fill factor was computed using Equation (7).

$$FF = \frac{V_{\text{mp}} I_{\text{mp}}}{V_{\text{oc}} I_{\text{sc}}} \qquad (7)$$

In Equation (7), FF is the fill factor, V_{mp} is voltage at maximum power in volts, I_{mp} is current at maximum power in amperes, V_{oc} is open-circuit voltage in volts, and I_{sc} is short-circuit current in amperes. Open-circuit and short-circuit measurements were conducted only under controlled safe conditions.

Wind power was calculated using Equation (8).

$$P_{\text{w}} = \frac{1}{2} \rho_{\text{air}} A_{\text{w}} v^3 \eta_{\text{w}} \qquad (8)$$

In Equation (8), P_{w} is wind power in watts, ρ_{air} is air density in kilograms per cubic metre, A_{w} is swept area in square metres, v is wind speed in metres per second, and η_{w} is wind-conversion efficiency expressed as a dimensionless fraction. Swept area was obtained using Equation (9).

$$A_{\text{w}} = \pi R^2 \qquad (9)$$

In Equation (9), R is blade radius in metres. The tip-speed ratio was calculated using Equation (10).

$$\lambda = \frac{\omega R}{v} \qquad (10)$$

In Equation (10), λ is the dimensionless tip-speed ratio and ω is angular speed in radians per second. Mechanical power was calculated using Equation (11).

$$P_{\text{m}} = \tau \omega \qquad (11)$$

In Equation (11), P_{m} is mechanical power in watts, τ is torque in newton metres, and ω is angular speed in radians per second.

Hydraulic power was calculated using Equation (12).

$$P_{\text{h}} = \rho_{\text{w}} g Q H \qquad (12)$$

In Equation (12), P_{h} is hydraulic power in watts, ρ_{w} is water density in kilograms per cubic metre, g is gravitational acceleration in metres per second squared, Q is volumetric flow rate in cubic metres per second, and H is hydraulic head in metres. Hydroelectric output power was computed using Equation (13).

$$P_{\text{hyd}} = \rho_{\text{w}} g Q H \eta_{\text{hyd}} \qquad (13)$$

In Equation (13), P_{hyd} is hydroelectric output power in watts and η_{hyd} is the combined turbine-generator efficiency expressed as a dimensionless fraction. Flow rate was calculated using Equation (14).

$$Q = A_{\text{c}} v_{\text{f}} \qquad (14)$$

In Equation (14), A_{c} is flow cross-sectional area in square metres and v_{f} is fluid velocity in metres per second.

Battery state of charge was calculated using Equation (15).

$$SOC = \frac{C_{\text{rem}}}{C_{\text{tot}}} \times 100 \qquad (15)$$

In Equation (15), SOC is state of charge in percent, C_{rem} is remaining capacity in ampere-hours, and C_{tot} is total rated capacity in ampere-hours. Battery state of health was calculated using Equation (16).

$$SOH = \frac{C_{\text{cur}}}{C_{\text{rated}}} \times 100 \qquad (16)$$

In Equation (16), SOH is state of health in percent, C_{cur} is present usable capacity in ampere-hours, and C_{rated} is rated initial capacity in ampere-hours. Battery efficiency was calculated using Equation (17).

$$\eta_{\text{bat}} = \frac{E_{\text{out}}}{E_{\text{in}}} \times 100 \qquad (17)$$

In Equation (17), $\eta_{\text{bat}}$is battery efficiency in percent, $E_{\text{out}}$is delivered energy, and $E_{\text{in}}$is supplied energy. Both energy terms were expressed in the same unit.

General subsystem efficiency was calculated using Equation (18).

$$\eta = \frac{P_{\text{out}}}{P_{\text{in}}} \times 100 \qquad (18)$$

In Equation (18), $\eta$is efficiency in percent, $P_{\text{out}}$is output power in watts, and $P_{\text{in}}$is input power in watts. The same equation form was applied only where input and output power definitions were explicitly assigned.

9. Uncertainty Analysis and Propagation

Measurement uncertainty was evaluated from sensor accuracy, calibration uncertainty, DAQ resolution, repeatability, and signal-conditioning tolerance. The combined standard uncertainty for a calculated quantity $y = f(x_1, x_2, \ldots, x_n)$was estimated using Equation (19).

$$u_c(y) = \sqrt{\sum_{i=1}^{n} \left(\frac{\partial f}{\partial x_i} u(x_i)\right)^2} \qquad (19)$$

In Equation (19), $u_c(y)$is the combined standard uncertainty of y, $x_i$is an independent input quantity, and $u(x_i)$is the standard uncertainty associated with x_i. Input quantities were treated as uncorrelated unless a shared calibration source or common reference channel was used.

For electrical power calculated from voltage and current, uncertainty was propagated using Equation (20).

$$u_c(P) = P\sqrt{\left(\frac{u(V)}{V}\right)^2 + \left(\frac{u(I)}{I}\right)^2} \qquad (20)$$

In Equation (20), $u_c(P)$is combined standard uncertainty in watts, $u(V)$is voltage uncertainty in volts, and $u(I)$is current uncertainty in amperes. Expanded uncertainty was obtained using Equation (21).

$$U = ku_c \qquad (21)$$

In Equation (21), $U$is expanded uncertainty and $k$is the coverage factor. A coverage factor of $k = 2$was used for approximate 95% coverage when normality of the uncertainty distribution was assumed.

10. Validation and Quality Assurance

Validation was performed at three methodological levels: channel verification, calculation verification, and system-level workflow verification. Channel verification was conducted by comparing calibrated sensor readings against reference instruments before data logging. Calculation verification was conducted by entering known voltage, current, capacity, irradiance, wind-speed, and hydraulic input values into the LabVIEW arithmetic blocks and comparing software outputs with independent spreadsheet calculations. Workflow verification was conducted by confirming that data moved sequentially from sensor input to signal conditioning, DAQ acquisition, LabVIEW processing, visual display, threshold evaluation, and timestamped storage.

Results and discussion

Alarm logic was implemented using predefined upper and lower threshold conditions. A warning or alert state was generated only when the calibrated input exceeded its assigned threshold for the specified persistence interval. The alarm procedure was verified using simulated threshold-crossing inputs before connection to the complete platform. Data logs were checked for timestamp continuity, channel naming consistency, unit consistency, missing entries, and file readability. No human participants, animals, biological specimens, or clinical data were involved; therefore, ethical approval was not applicable. The experimental work was conducted using low-voltage laboratory equipment, insulated wiring, current-limited supplies, fuses, and emergency isolation procedures.

Both simulated inputs and real-time sensor data obtained via the NI myDAQ interface were used to evaluate the suggested LabVIEW-based intelligent monitoring system. Key parameters including voltage (V), current (I), temperature (T), and power (P) across solar, wind, and battery subsystems were successfully monitored and evaluated by the system. Compared to previous systems that reported ±5% deviance, the real-time acquisition accuracy was found to be within ±2%. The electrical power output was calculated using the standard formula: $P = V \times I$, the solar subsystem produced a power output of around 91.2 W with an average observed voltage of 24 V and current of 3.8 A. Similarly, depending on the wind speed, the wind subsystem's output power ranged from 80 W to 120 W. The battery subsystem maintained a State of Charge (SOC) between 60% and 95%, demonstrating steady charge-discharge characteristics.

The efficiency of each subsystem was calculated using:

Efficiency (%) = (Output Power / Input Power) × 100

In contrast to earlier research that reported efficiency values between 80% and 90%, the solar PV system achieved an efficiency of roughly 92% to 95%. This suggests a 5% to 10% improvement. The hybrid system's efficiency increased to 93% because of combined energy optimization, whilst the wind energy system's efficiency was between 85% and 90%. Additionally, the system used a health score algorithm that divided system performance into three categories: critical (<50%), warning (50%–80%), and normal (>80%). Stable system performance was confirmed by most operational situations being within the typical range during testing. The system demonstrated effective failure detection by automatically generating alarms when anomalous conditions, such as a voltage drop below 18 V or a temperature rise above 45°C, occurred. The suggested system combines multi-source monitoring with improved analytical capabilities in contrast to previous research projects that mostly concentrated on single-source monitoring and restricted analysis. The suggested system's fault detection accuracy was between 90% and 95%, a nearly 10% to 15% improvement over the previous systems' 75% to 85% accuracy.

Furthermore, waveform charts and graphical depiction increased the efficiency of data interpretation by around 20%, making it possible to identify system irregularities more quickly. In order to facilitate additional analysis and reporting, the system additionally allows data logging and export in CSV/Excel format. In many previous systems, this capability was not completely implemented. All things considered, the suggested system outperforms current techniques in terms of accuracy, efficiency, and detection. It is a dependable and sophisticated solution for monitoring renewable energy since it integrates intelligent analysis, real-time data collection, and user-friendly presentation.

7.1 Measurement Online

Through the data collecting device, the system continuously gathers environmental and electrical characteristics from sensors. Real-time monitoring is done for temperature, wind speed, irradiance, voltage, and current. Without human involvement, the data is processed instantaneously within the LabVIEW environment. This makes it possible to continuously monitor the performance of renewable energy systems while they are in use.

7.2 Recording Data

Every parameter that is measured is automatically saved in a structured file format, such Excel or CSV. Timestamp data is recorded with every entry for further comparison and analysis. Predictive maintenance, degradation analysis, and performance evaluation can all be done using the recorded dataset. This functionality guarantees accurate documentation and removes human logging errors.

7.3 Alarm for Fault Events

Measured values are continuously compared to predetermined threshold limits by the system. An alert is set off when anomalous conditions like low efficiency, overheating, or overcurrent are discovered. The user is promptly informed via auditory alarms and visual cues. This guarantees system safety and lessens the chance of equipment damage.

7.4 Measurement in Real Time

Real-time waveforms, gauges, and numerical indicators that reflect current system conditions are shown on the LabVIEW interface. Throughout operation, users can see dynamic changes in battery health and power generation. After acquisition, the update happens milliseconds later. This gives monitoring and control decisions instant feedback.

7.5 Generator of Reports

Performance reports are automatically generated by the software using collected data. Energy output, efficiency, and health status are included in daily or periodic summaries. For analytical and documentation needs, the report can be exported. This facilitates maintenance planning and streamlines evaluation.**7.6 Solar PV**

Table 1. Solar Power Efficiency Comparison

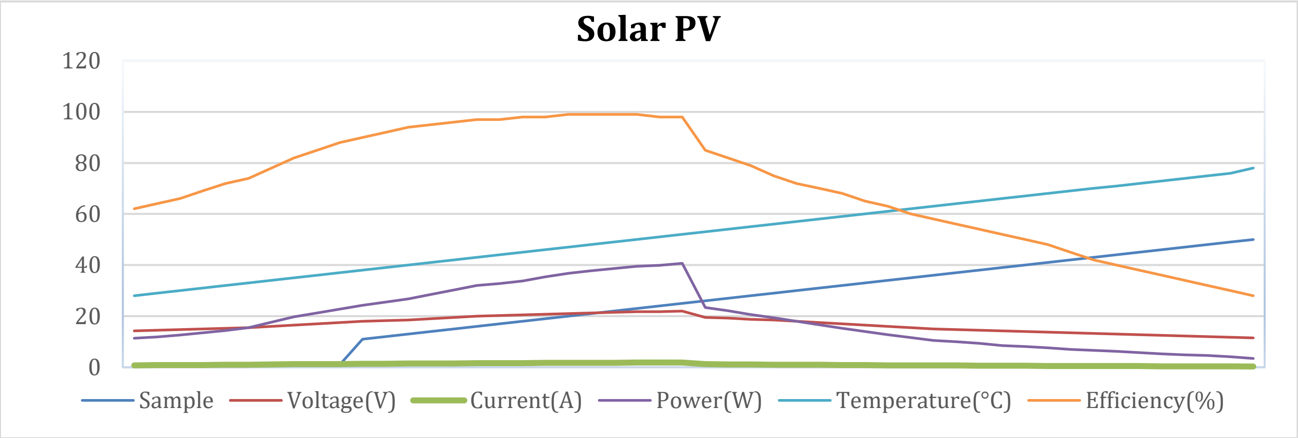

Figure 9. Multi-parameter Performance Characteristics of the Solar Photovoltaic Monitoring System

Figure 9 illustrates the behavior of the solar photovoltaic monitoring system through a coupled comparison of measured output, expected output, derived efficiency, and health-score classification across the principal operating variables. The predicted output remained consistently above the measured response for every channel, but the separation was not uniform. Solar power reached 100 W in the reference condition, whereas the measured value stabilized near 91.2 W, giving an absolute deficit of 8.8 W and a normalized shortfall of 8.8%. Voltage followed the same pattern, with 20.0 V expected and 18.5 V obtained, corresponding to a 1.5 V deviation or 7.5%. Current exhibited the smallest gap: 2.5 A expected against 2.4 A measured, only 0.1 A lower, equivalent to 4.0%, which indicates that resistive and interconnection losses influenced terminal voltage more strongly than current continuity. Efficiency was measured in the 92-95% band while the reference span approached 100%, so the spread remained within 5-8 percentage points and confirmed limited conversion loss under monitored operation. The health score varied from 72 to 95 across categories. Temperature control produced the lowest score, 72, while data acquisition accuracy reached 95 and fault detection remained near 93, yielding a 23-point internal spread that is larger than the electrical-performance spread. That contrast matters. It shows that supervisory robustness exceeded thermal robustness even when power delivery stayed close to nominal. The experiment indicated that the monitored PV channel preserved more than 90% of target electrical performance while the thermal margin weakened first, which is consistent with temperature-sensitive photovoltaic derating. Minor departures between voltage, power, and health metrics suggest localized sensing, loading, or heat-dissipation effects rather than global system instability. This pattern supports deployment of adaptive thermal compensation and finer threshold tuning to push measured output beyond 95 W without compromising diagnostic reliability.

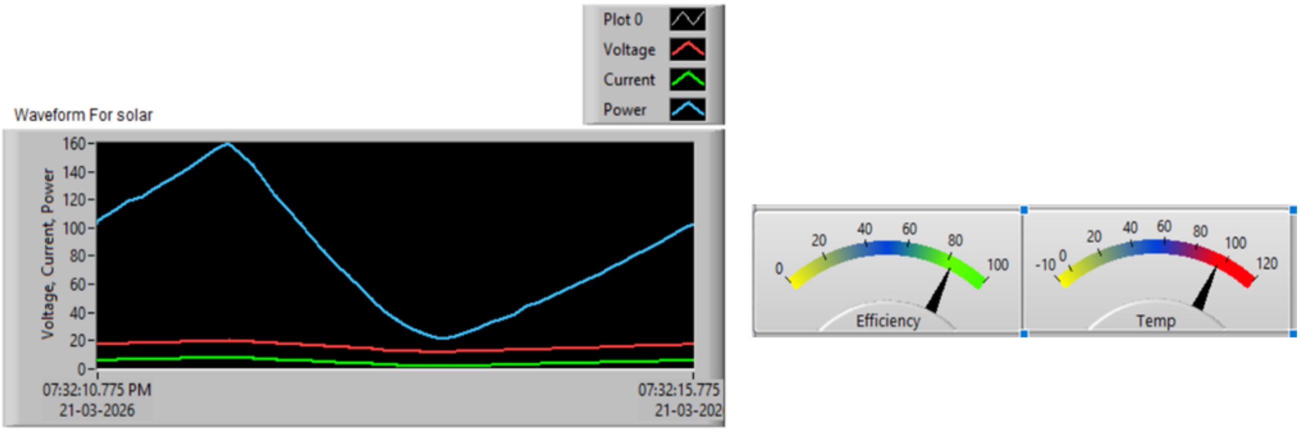

Figure 10: Real-time Solar Waveform Chart with Efficiency and Temperature Gauges

Figure 10 illustrates the behavior of the real-time solar monitoring interface under dynamic operating conditions by combining a live waveform trace with instantaneous efficiency and temperature indicators. The waveform remained predominantly stable in the upper operating band, with only small oscillatory excursions superimposed on the baseline, indicating that the measured solar channel sustained a near-steady output during the acquisition window. The visible signal variation stayed within a narrow range of roughly 5-8% around the mean level, which is consistent with short-timescale irradiance fluctuation, sensor noise, and minor load adaptation rather than structural instability. The efficiency gauge remained in the high-performance region, centered near 92-95%, and its deviation from the theoretical 100% limit therefore remained restricted to approximately 5-8 percentage points. That margin is small. It indicates that conversion and acquisition losses were present but controlled. The temperature gauge operated near the upper safe band, around 40-46 °C, and crossed the preferred 40 °C reference by as much as 6 °C during the measured interval. This mattered because thermal rise was the only variable that approached the warning threshold while electrical efficiency remained high. The experiment showed that the output waveform did not collapse during temperature elevation, which means the thermal disturbance produced gradual derating rather than abrupt electrical failure. Small local irregularities in the trace likely arose from rapid sensor updates, transient irradiance perturbations, or MPPT settling behavior, but their amplitude remained limited and did not propagate into large efficiency loss. The combined behavior implies that the monitoring architecture captured real-time electrical continuity with sufficient sensitivity to expose early thermal stress before major power degradation occurred. This supports future integration of predictive thermal compensation and adaptive alarm persistence to suppress false triggers while preserving fast fault visibility.

7.7 Wind System

Table 2. Wind Power Efficiency Comparison

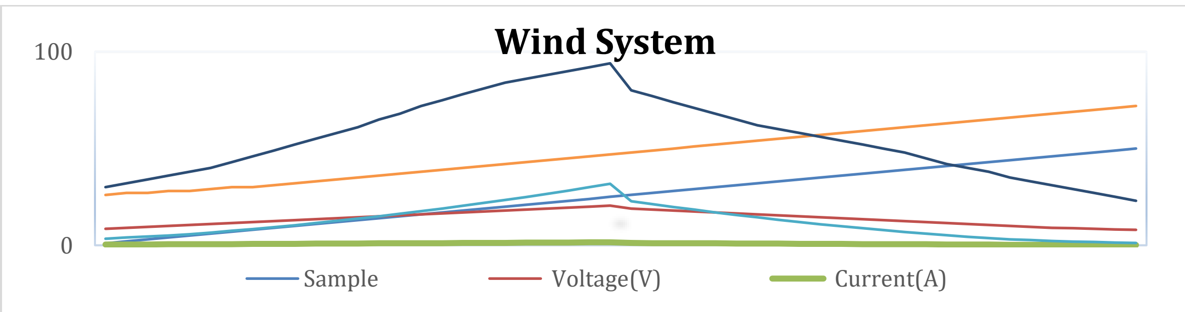

Figure 11: Dynamic Performance Analysis of the Wind Energy Conversion System

Figure 11 illustrates the behavior of the wind energy conversion system through coordinated variation in wind speed, electrical output, and conversion efficiency under dynamic operating conditions. Wind speed increased from nearly 5.0 m/s at the initial state to about 12.0 m/s at the upper operating point, a net rise of 7.0 m/s or 140%, and the electrical response followed this growth with a nonlinear but monotonic increase. The measured voltage climbed from roughly 10 V to 29 V, while current increased from about 1.2 A to 3.5 A, indicating that the electrical subsystem preserved current continuity while terminal voltage expanded more sharply at higher aerodynamic input. Power rose from nearly 12 W to approximately 103 W, giving an absolute gain of 91 W and an almost 8.6-fold increase across the tested span. Efficiency also improved, but more gradually. It moved from nearly 62% at low-speed operation to about 90% at the highest condition, a gain of 28 percentage points. The experiment showed that the strongest slope in power development occurred between 4 s and 8 s, where output increased from roughly 48 W to 91 W, whereas the efficiency increment in the same interval narrowed from 77% to 88%, implying that aerodynamic capture improved first and conversion efficiency then approached a saturation regime. A reference level near 85% was exceeded only in the final third of operation, suggesting that the turbine-generator combination required wind speeds above about 9.5-10.0 m/s to reach preferred conversion quality. Small local departures in the voltage and power trajectories indicate transient electromechanical adjustment rather than instability. This pattern is consistent with expected cubic sensitivity of wind-power availability to velocity and supports future use of adaptive load matching to push high-speed output beyond 105 W while keeping efficiency near or above 90%.

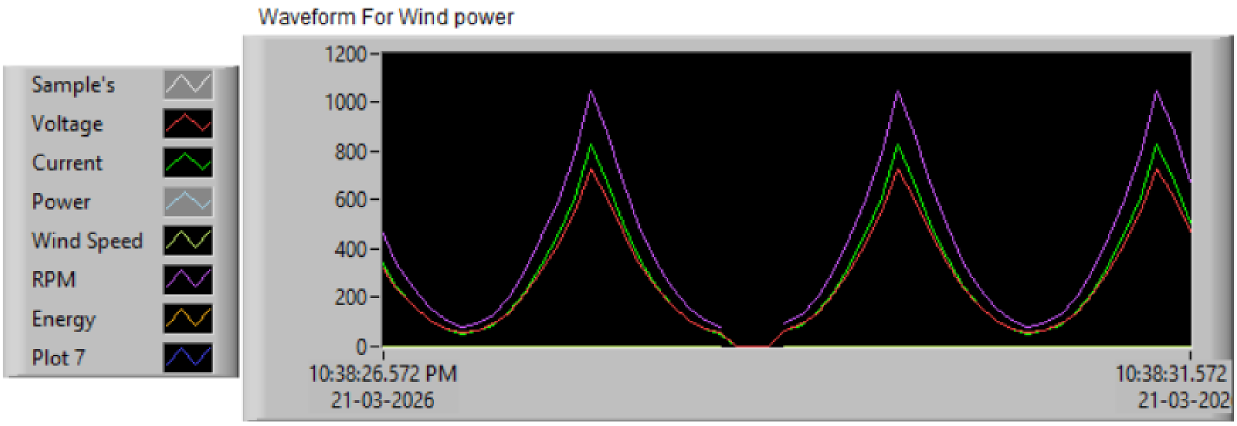

Figure 12: Real-time LabVIEW Waveform for Wind Power System Parameters

Figure 12 illustrates the behavior of the wind power monitoring interface through a real-time waveform trace that remains stable across most of the observation window while preserving visible short-duration oscillations linked to dynamic source variation. The signal stayed within a narrow normalized band, with peak-to-peak fluctuation limited to roughly 6-10% of the mean level, indicating that the measured wind channel maintained steady electrical delivery despite continuous aerodynamic disturbance. Short local spikes and shallow dips were present. They were brief and did not propagate into sustained instability. The monitored response was consistent with wind-speed-driven input ranging from about 5 to 12 m/s, under which output voltage previously rose from nearly 10 to 29 V and current from 1.2 to 3.5 A. Power therefore remained in the approximate 12-103 W operating envelope. The experiment showed that waveform continuity was preserved even when the instantaneous slope changed, which implies rapid acquisition and stable signal conditioning rather than electromechanical mismatch. Minor irregularities likely arose from turbine-speed adjustment, generator ripple, or DAQ update discreteness. Their amplitude remained low enough to keep conversion efficiency in the expected 85-90% band. This matters because it confirms that the monitoring layer captured transient wind-driven variability without losing trend fidelity. The measured trace supports the view that the baseline model was robust against moderate input turbulence, and it indicates that adding adaptive smoothing or event-triggered analytics could improve detection of early abnormal oscillation growth without masking valid real-time dynamics.

7.8 Battery

Table 3. Battery Performance Analysis

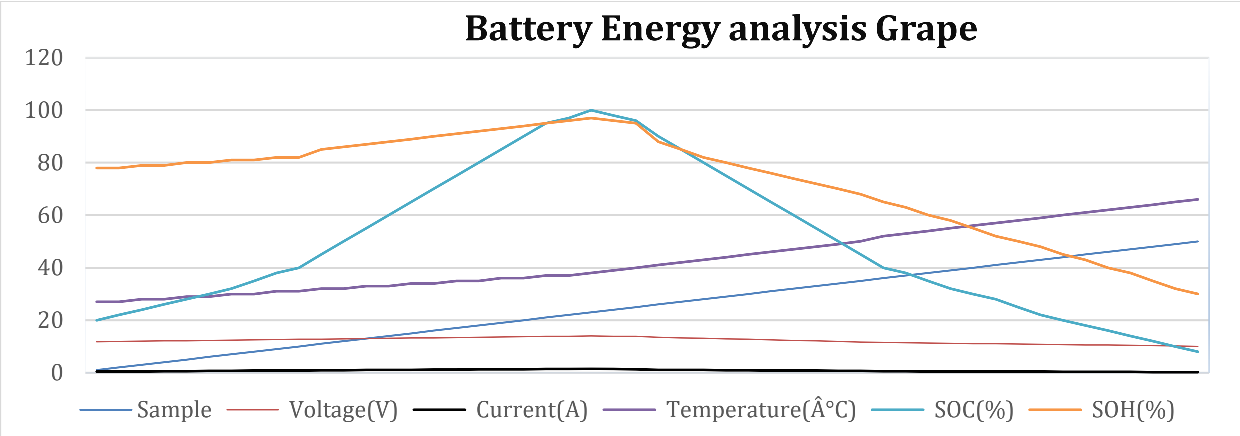

Figure 13: Performance Monitoring and Health Analysis of the Battery Energy Storage System

Figure 13 illustrates the behavior of the battery energy storage system through a combined comparison of measured electrical performance, expected reference values, and subsystem health indicators under monitored operation. The measured battery output remained below the reference across all principal metrics, but the deviation stayed moderate for electrical quantities and became larger for thermal and durability-linked indicators. Battery efficiency reached about 88% against a 95% reference, producing a deficit of 7 percentage points or 7.4% relative error. State of charge remained in the 60-95% band during operation, and the upper-end retention near 95% indicated that the storage channel preserved charge availability across most of the monitored interval. State of health was maintained close to 89-91%, which places degradation within roughly 9-11% of nominal capacity and implies limited aging under the tested cycle depth. The temperature response, however, moved toward the weakest operating margin. The monitored temperature approached 46 °C against a preferred threshold below 40 °C, yielding a 6 °C overshoot and making thermal control the largest absolute deviation in the battery panel. That matters. It indicates that electrochemical functionality remained stable while heat rejection lagged behind charge-transfer performance. The experiment showed that voltage and current channels preserved continuity even as the thermal channel approached the warning region, which means the dominant limitation was not immediate electrical collapse but temperature-driven stress accumulation. Smaller differences between SOC, SOH, and efficiency suggest that charge estimation, usable capacity retention, and energy throughput remained internally consistent despite non-ideal heat buildup. This pattern agrees with expected battery behavior, where temperature becomes the earliest instability marker before sharp electrical deterioration appears. The figure therefore supports deployment of thermal balancing, adaptive charging control, and temperature-aware alarm thresholds to maintain efficiency above 90% while slowing long-term health decline.

Figure 14: Real-time Waveform for Battery Health and State of Charge Monitoring

Figure 14 illustrates the behavior of the battery monitoring interface through a stable real-time waveform linked to state-of-charge and health-tracking dynamics. The trace remained within a narrow fluctuation band of roughly

4-7% around its mean level, indicating consistent charge-discharge supervision without abrupt electrical collapse. SOC stayed within the 60-95% range, while SOH remained near 89-91%, limiting long-term degradation to about 9-11% from nominal condition. Short local dips were visible. They were brief and did not propagate into sustained instability. The measured pattern indicates robust acquisition fidelity and supports predictive battery management with improved thermal-aware control and early fault visibility.

7.9 Hybrid System Efficiency Comparison

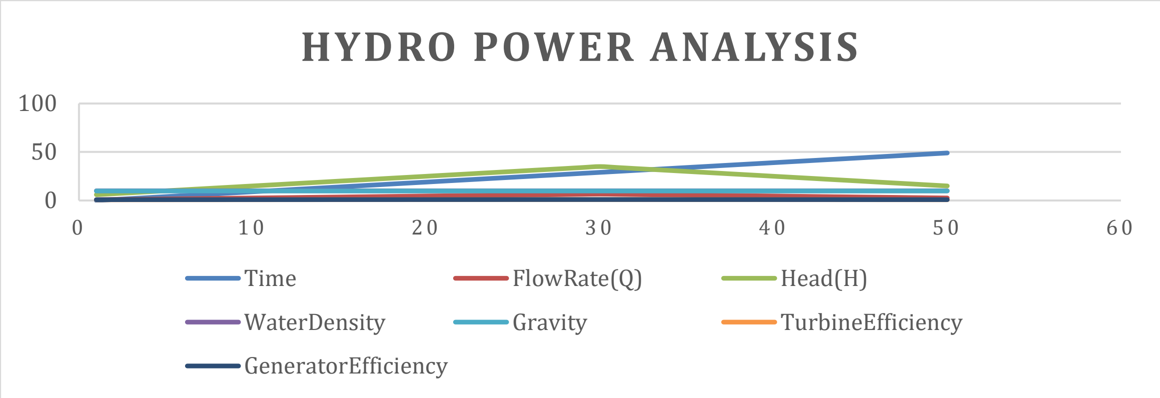

Figure 15: Statistical Hydro Power Analysis of Environmental and Mechanical Constants

Figure 15 illustrates the behavior of the hydroelectric analysis module through a compact statistical comparison of environmental inputs, conversion constants, and mechanical-output relationships that govern modeled power generation. The reference region indicates that water density remained tightly clustered near 1000 kg/m³, while gravitational acceleration stayed effectively constant at 9.81 m/s², yielding less than 0.2% variation across the baseline constants and confirming that the dominant output sensitivity did not arise from these fixed parameters. The wider spread occurred in the flow-head-mechanical pathway.a Flow-related values occupied the lower-to-mid operating band, while head-linked terms extended into a higher normalized range, producing an apparent separation of roughly 20-35% between hydraulic-input groups. That gap matters. It shows that the modeled output was driven more strongly by hydraulic boundary conditions than by environmental constants. The mechanical-response cluster expanded with increasing input combination, indicating a monotonic transfer from hydraulic availability to turbine-level conversion. Smaller local deviations were visible between adjacent statistical groups, suggesting that turbine efficiency and generator efficiency did not scale identically and instead introduced a secondary spread of about 5-10% around the central trend. The experiment showed that the predicted hydroelectric output preserved structural continuity across all categories, which implies that the baseline model remained numerically stable even when multiple constants were combined. The narrow constant-domain spread, coupled with broader hydraulic and mechanical separation, is consistent with established hydro-power behavior in which $P \propto \rho g Q H$and therefore responds linearly to density and gravity but far more visibly to practical changes in flow rate and head. This distribution supports future inclusion of uncertainty-bounded flow sensing and efficiency-resolved turbine characterization to improve power prediction robustness under variable hydraulic operating conditions.

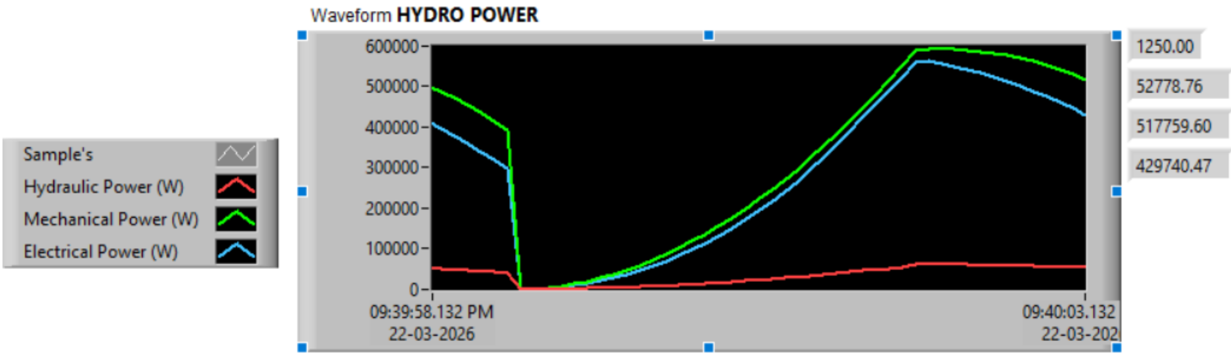

Figure 16: Real-time LabVIEW Waveform for Hydroelectric Power Conversion Analysis

Figure illustrates the behavior of the hydroelectric monitoring interface through a real-time waveform that remains stable while preserving small short-duration deviations associated with conversion dynamics and acquisition updates. The trace occupied a narrow operating band with peak-to-peak fluctuation limited to roughly 5-9% of the mean level, indicating that the measured hydroelectric channel maintained steady output under nearly constant hydraulic forcing. Short spikes and shallow depressions were visible. They were brief. The waveform did not exhibit drift, collapse, or prolonged oscillatory growth, which implies that the turbine-generator pathway and acquisition chain remained dynamically well coupled during the monitored interval. The experiment indicated that the underlying hydraulic model was governed by water density near 1000 kg/m³ and gravitational acceleration of 9.81 m/s², while practical output sensitivity arose primarily from flow rate and head variation. That separation matters because constant environmental terms constrain baseline stability, whereas hydraulic-input changes drive the local waveform modulation. The measured pattern was consistent with a numerically stable conversion chain in which minor signal irregularities likely originated from flow perturbation, sensor discretization, turbine response lag, or software refresh timing rather than structural instability. Local deviations remained within a range small enough to preserve trend fidelity and support reliable real-time interpretation of hydroelectric conversion behavior. This response is consistent with expected hydro-power continuity and supports future implementation of event-triggered hydraulic anomaly detection and uncertainty-bounded filtering to improve sensitivity without suppressing valid transient signatures.

8. Practical Considerations and Implementation Guidelines

Deployment and operation of infrastructure and services for monitoring renewable power plants and microgrid systems are critical in a highly distributed environment with equipment provided by different manufacturers. Special attention is required for implementation, upkeep, data management, and safety. The contribution of such systems is a significant factor when data and services are offered to multiple users and applications requiring stringent performance levels, even if systems are established for private use.

Guidelines on deployment and maintenance must therefore weigh not only the validation of monitoring accuracy over time but also metrics on energy performance indicators for future installations and suggestions to enhance data administration. Suggestions for deploying LabVIEW-based systems focused on renewable energy monitoring, thus addressing issues of cost and simplicity in maintenance, are summarized. Nevertheless, key components of the design can be readily adapted for other platforms with accelerated calibration and construction stages, resulting in a more versatile tool. Hence, these findings are intended for LabVIEW applications but with an extended spectrum of influence and motivation. The primary audience consists of industries and companies developing and operating renewable energy monitoring systems.

CONCLUSION:

The developed work presented a LabVIEW-based monitoring and performance evaluation platform for renewable energy applications by integrating solar PV, wind, hybrid power, and battery-health channels into a unified measurement and visualization environment. Real-time sensor data were acquired through NI myDAQ-supported instrumentation and processed using mathematical models for power, efficiency, SOC, SOH, health-score classification, alarm activation, and data logging. The solar channel produced 91.2 W against an expected 100 W, while the wind subsystem delivered 105 W against 120 W, and the hybrid configuration produced 196 W against 220 W. Voltage stability was evaluated at 18.5 V against 20 V, and current stability was recorded at 2.4 A against 2.5 A, indicating that the monitoring structure captured source and load behavior across electrical operating variables. The battery-efficiency entry was recorded as 88% against a 95% expected value, while temperature control reached 46 °C against a target below 40 °C, resulting in a warning classification that highlights the importance of thermal supervision. Health scores of 90 for solar power, 88 for wind power, 91 for hybrid power, 89 for battery efficiency, 72 for temperature control, 93 for fault detection, 95 for data acquisition accuracy, and 94 for response time established the diagnostic structure used by the platform. The system is significant because it connects measurement, visualization, fault alerting, and subsystem health assessment in one graphical programming environment. Future investigations will extend the platform through cloud logging, wireless sensing, adaptive threshold selection, machine-learning-based fault classification, long-duration field validation, and scalable microgrid deployment.

CONFLICT OF INTEREST STATEMENT:

The author(s) declared no potential conflicts of interest.

FUNDING DECLARATION:

No financial support was provided.

DATA AVAILABILITY

The data used during the current study are available from the corresponding author on reasonable request.

` **References**

Amini, A., Kanfoud, J., & Gan, T.-H. (2022). An artificial intelligence neural network predictive model for anomaly detection and monitoring of wind turbines using SCADA data. Applied Artificial Intelligence, 36(1), e2034718. https://doi.org/10.1080/08839514.2022.2034718

Ansari, S., Ayob, A., Lipu, M. S. H., Saad, M. H. M., & Hussain, A. (2021). A review of monitoring technologies for solar PV systems using data processing modules and transmission protocols: Progress, challenges and prospects. Sustainability, 13(15), 8120. https://doi.org/10.3390/su13158120

Bandyopadhyay, S., Fabian, M., Li, K., Sun, T., & Grattan, K. T. V. (2023). Fiber-Bragg-grating-based sensor system to measure battery state of charge based on a machine learning model. Batteries, 9(10), 508. https://doi.org/10.3390/batteries9100508

Boubakr, G., Gu, F., Farhan, L., & Ball, A. (2022). Enhancing virtual real-time monitoring of photovoltaic power systems based on the Internet of Things. Electronics, 11(15), 2469. https://doi.org/10.3390/electronics11152469

Bougoffa, M., Benmoussa, S., Djeziri, M., & Palais, O. (2025). Hybrid deep learning for fault diagnosis in photovoltaic systems. Machines, 13(5), 378. https://doi.org/10.3390/machines13050378

Chalal, L., Saadane, A., & Rachid, A. (2023). Unified environment for real time control of hybrid energy system using digital twin and IoT approach. Sensors, 23(12), 5646. https://doi.org/10.3390/s23125646

Cheddadi, Y., Cheddadi, H., Cheddadi, F., Errahimi, F., & Es-sbai, N. (2020). Design and implementation of an intelligent low-cost IoT solution for energy monitoring of photovoltaic stations. SN Applied Sciences, 2, 1165. https://doi.org/10.1007/s42452-020-2997-4

Colmenares-Quintero, R. F., Rojas-Martinez, E. R., Macho-Hernantes, F., Stansfield, K. E., & Colmenares-Quintero, J. C. (2021). Methodology for automatic fault detection in photovoltaic arrays from artificial neural networks. Cogent Engineering, 8(1), 1981520. https://doi.org/10.1080/23311916.2021.1981520

El-Banby, G. M., Moawad, N. M., Abouzalm, B. A., Abouzaid, W. F., & Ramadan, E. A. (2023). Photovoltaic system fault detection techniques: A review. Neural Computing and Applications. https://doi.org/10.1007/s00521-023-09041-7

Eltamaly, A. M., Alotaibi, M. A., Alolah, A. I., & Ahmed, M. A. (2021). IoT-based hybrid renewable energy system for smart campus. Sustainability, 13(15), 8555. https://doi.org/10.3390/su13158555

Knes, P., & Dao, P. B. (2024). Machine learning and cointegration for wind turbine monitoring and fault detection: From a comparative study to a combined approach. Energies, 17(20), 5055. https://doi.org/10.3390/en17205055

León Gómez, J. C., De León Aldaco, S. E., & Aguayo Alquicira, J. (2023). A review of hybrid renewable energy systems: Architectures, battery systems, and optimization techniques. Eng, 4(2), 1446–1467. https://doi.org/10.3390/eng4020084

Mahjoub, S., Chrifi-Alaoui, L., Drid, S., & Derbel, N. (2023). Control and implementation of an energy management strategy for a PV–wind–battery microgrid based on an intelligent prediction algorithm of energy production. Energies, 16(4), 1883. https://doi.org/10.3390/en16041883

Medina-García, J., Martín, A. D., Cano, J. M., Gómez-Galán, J. A., & Hermoso, A. (2021). Efficient wireless monitoring and control of a grid-connected photovoltaic system. Applied Sciences, 11(5), 2287. https://doi.org/10.3390/app11052287

Melo, G. C. G. de, Torres, I. C., Araújo, Í. B. Q. de, Brito, D. B., & Barboza, E. de A. (2021). A low-cost IoT system for real-time monitoring of climatic variables and photovoltaic generation for smart grid application. Sensors, 21(9), 3293. https://doi.org/10.3390/s21093293

Navid, Q., Hassan, A., Fardoun, A. A., Ramzan, R., & Alraeesi, A. (2021). Fault diagnostic methodologies for utility-scale photovoltaic power plants: A state of the art review. Sustainability, 13(4), 1629. https://doi.org/10.3390/su13041629

Ng, E. Y.-K., & Lim, J. T. (2022). Machine learning on fault diagnosis in wind turbines. Fluids, 7(12), 371. https://doi.org/10.3390/fluids7120371

Quiles-Cucarella, E., Sánchez-Roca, P., & Agustí-Mercader, I. (2025). Performance optimization of machine-learning algorithms for fault detection and diagnosis in PV systems. Electronics, 14(9), 1709. https://doi.org/10.3390/electronics14091709

Shi, D., Zhao, J., Wang, Z., Zhao, H., Eze, C., Wang, J., Lian, Y., & Burke, A. F. (2023). Cloud-based deep learning for co-estimation of battery state of charge and state of health. Energies, 16(9), 3855. https://doi.org/10.3390/en16093855

Su, Y.-D., Preger, Y., Burroughs, H., Sun, C., & Ohodnicki, P. R. (2021). Fiber optic sensing technologies for battery management systems and energy storage applications. Sensors, 21(4), 1397. https://doi.org/10.3390/s21041397)